Diao, F., Xiong, X., Wang, R. (2011): Mechanisms of transient postseismic deformation following the 2001 Mw 7.8 Kunlun (China) earthquake. - Pure and Applied Geophysics, 168, 5, 767-779

DOI: 10.1007/s00024-010-0154-5

Mechanisms of transient postseismic deformation following the 2001 Mw 7.8 Kunlun earthquake in China

FAQI DIAO[1, 2], XIONG XIONG[1], and RONGJIANG WANG[3]

[1] Key Laboratory of Dynamic Geodesy, Institute of Geodesy and Geophysics, Chinese Academy of Sciences, Wuhan 430077, China

[2] Graduate University, Chinese Academy of Sciences, Beijing 100038, China

[3] GFZ German Research Centre for Geosciences, D-14473 Potsdam, Germany

Abbreviated title: Afterslip, viscoelastic relaxation of Kunlun event

Corresponding author: Faqi Diao

Address: Institute of Geodesy and Geophysics, Chinese Academy of Sciences,
Wuhan 430077, China

Phone: +86 (27) 68881314

Fax: +86 (27) 86783841

E-mail: faqidiao@asch.whigg.ac.cn

Abstract

Using the Global Positioning System (GPS) technique, significant postseismic surface displacements have been observed within the first four months after the 2001 Mw 7.8 Kunlun earthquake which occurred in China. In this study, we investigated the possible mechanisms that may have contributed to the postseismic deformations that have been observed. Based on the modeling results, we find that an afterslip model can interpret postseismic displacements in the near field even when the fault plane is extended to the bottom of the crust (~70 km). Models based on the viscoelastic relaxation theory showed a large discrepancy in the spatial pattern of the deformation compared with what has been observed. Thus, we infer that both mechanisms cannot interpret the observed postseismic deformation independently. A combination of afterslip and viscoelastic relaxation can further improve the data fit, especially at sites far from the fault. With maximum afterslip of ~0.4 m occurring at the depth of 10 km in the central section, the combined model shows that the estimated afterslip mostly occurred on and below the coseismic rupture plane, as well as on its eastern extension. The estimated moment released by the afterslip in the first four months is almost 40% of that released by the coseismic slip. The best-fitting viscoelastic relaxation model shows a "weak" upper mantle with a viscosity of ~1.0×10^{18} Pa s. The combined model also prefers a lower crust with viscosity larger than 1.0×10^{18} Pa, although it cannot be constrained accurately.

Keywords: the Kunlun earthquake, GPS, postseismic deformation, viscoelastic relaxation, afterslip

1. Introduction

Using high-precision space geodetic techniques, postseismic deformations induced by coseismic stress loading have been observed following many large earthquakes (e.g., SHEN *et al*., 1994; REILINGER *et al*., 2000; RYDER *et al*., 2007). Investigations on observed postseismic response can provide new insights into fault behavior and regional rheology, which are essential in gaining an improved understanding of fault dynamic evolution and the crust-mantle coupling in driving continental deformation. However, due to different geological environments surrounding a seismogenic fault, the mechanisms behind postseismic responses are likely to be specific to each earthquake (SAVAGE and SVARC, 1997; DENG *et al*., 1998; POLLITZ *et al*., 2000; REILINGER *et al*., 2000; RYDER *et al*., 2007).

Various mechanisms have been reported as being responsible for the observed postseismic deformations. For example, poroelastic rebound, which is induced by the fluid flow in the upper crust due to coseismic pore pressure changes, has been found to take effect within a small scale near the fault (PELTZER *et al*., 1998; JÓNSSON *et al*., 2003), while viscoelastic relaxation, which releases the coseismic stress loading by viscous flow in the lower crust and the upper mantle, has been found to be the dominant mechanism for postseismic motions with long wavelength deformation pattern and large time scale (POLLITZ *et al*., 2000; POLLITZ, 2005; FREED *et al*., 2007). Afterslip, which mostly occurs on the coseismic rupture plane or its extension (where the fault is temporally locked or partially ruptured in the coseismic rupture process), is generally responsible for postseismic deformations in the source area with a short wavelength deformation pattern. (REILINGER *et al*., 2000; HSU *et al*., 2002; MIYAZAKI *et al*., 2004; FREED, 2007). However, results from different studies indicated that no single mechanism can be applied to all case studies. This means that more than one process may occur in any individual case.

Figure 1

The Tibet Plateau is a large, active orogenic zone, and is generally regarded as a natural laboratory for continental dynamics studies. The Mw 7.8 Kunlun earthquake occurred on November 14, 2001, rupturing the Kunlun fault in a region of northeastern Tibet. As the seismogenic fault of the Kunlun earthquake, the Kunlun fault is one of the main left-lateral

strike-slip fault systems that run across the Tibetan plateau (Fig. 1). Based on Global Positioning System (GPS) measurements, a study has found that the Kunlun fault adjusted the eastward motion of the Qiangtang block in the south with respect to the Qaidam basin in the north, with a decadal slip rate of ~1 cm/yr (WANG *et al*., 2001). With a rupture length of up to 400 km, the Kunlun earthquake exhibited a clear characteristic of a left-lateral strike-slip (LIN *et al*., 2002; KLINGER *et al*., 2005; XU *et al*., 2006). In addition, this earthquake is widely considered as the consequence of the continuing collision of the India plate to the Eurasia plate, as well as the eastward extrusion of Tibet. A previous study (LASSERRE *et al*., 2005) inverted the coseismic slip model from the InSAR (Interferometric Synthetic Aperture Radar) observation and indicated that the maximum coseismic slip is up to 8 m, with slip concentrations mostly located at shallow depths of less than 20 km (Fig. 2a).

REN and WANG (2005) and QIAO *et al*. (2002) reported on the postseismic GPS displacements, but they did not provide any further analysis of the driving source based on numerical modeling. Constrained by the GPS displacement time series at four stations, ZHANG *et al*. (2007) simulated the postseismic process using the Maxwell solid and pointed out that the viscosity of the lower crust is in the order of ~10^{17} Pa s. SHAO *et al*. (2008) investigated the effect of viscoelastic relaxation based on finite element modeling and concluded that the viscosities of the lower crust on the south and north sides of the Kunlun fault are 5.0×10^{17} and 9.0×10^{18} Pa s, respectively. However, all previous postseismic studies on the Kunlun earthquake did not consider the effect of afterslip, which is often found to be significant in the initial period of the postseismic process (e.g., REILINGER *et al*., 2000; HSU *et al*., 2002).

This study aims to interpret the initial four-month postseismic displacements following the 2001 Mw 7.8 Kunlun earthquake and thus take insights into the regional rheological structure, as well as the evolution of the Kunlun fault. Preliminary modeling showed clear contrast with a poroelastic model, based on the observed postseismic displacements of the Kunlun earthquake. We therefore focused our analysis on afterslip and the viscoelastic relaxation of the lower crust and the upper mantle.

2. Data

The region surrounding the Kunlun earthquake is a depopulated area with high altitude and

adverse weather condition, making field data collection extremely difficult. Therefore, only few postseismic observations were carried out after the earthquake even if it occurred more than eight years ago. At present, only two data sets have been published, which are essential in undertaking postseismic studies of the Kunlun earthquake. One refers to the postseismic displacements measured during the first four months after the earthquake (QIAO *et al*., 2002), and the other refers to the first one-year displacement times series at four GPS sites in the east-west direction (REN and WANG, 2005). Postseismic displacements in the initial four months were used as surface constraint in this study, while the one-year displacement time series was cited for further analysis of our modeling results.

The observation and data processing of the two data sets have already been described in detail in previous papers (QIAO *et al*., 2002; REN and WANG, 2005). Therefore, we only briefly present here the data that have been utilized in this study. The postseismic displacements at 15 campaign-surveyed stations published by QIAO *et al*. (2002) were the results of observations of the two sessions held on November 2001 and March 2002. Using Ashtech Z-12 geodetic receivers with choke-ring antennas, each session consisted of 36-hour to 72-hour observations. Most of the stations were pre-existing and were built over the bedrock. The collected carrier phase observations were processed with the GIPSY/OASIS-II software using a regional strategy (WANG *et al*., 2001). Fixed orbits and satellite clocks provided by NASA's Jet Propulsion Laboratory were adopted in the data processing. Following a "non-fiducial" strategy, a loosely constrained daily solution was initially obtained, which was transformed into the ITRF97 (International Terrestrial Reference Frame 1997) by subsequently estimating the seven-parameter transformation. In addition, the secular motions estimated from the preseismic observations from 1991 to 2001 were removed from the obtained postseismic displacements. The continuous observations at four GPS sites (REN and WANG, 2005) were also collected using Ashtech Z-12 geodetic receivers, and the secular motions included in the time series were removed using the same strategy as that used by QIAO *et al*. (2002). The data set from the continuous observation was processed using the GAMIT/GLOBK software. The loosely constrained daily solution resulting from the GAMIT software was transformed into ITRF2000 using the GLOBK software. Although the two data sets were fixed to different reference frames (i.e., ITRF97 and ITRF2000), the induced no-self-consistency between them was negligible compared with the difference induced by the model simplification in this study.

The observed postseismic displacements (Fig. 4, black arrows) show clear left-lateral motion. Additionally, with a maximal displacement of up to ~10 cm, the displacements decreased along with the increasing distance from the fault. In addition, the data set covers an area from ~10 km to ~400 km from the fault, providing both near-field and far-field constraints in our modeling.

3. Afterslip Model

Afterslip is responsible for postseismic deformations following several large strike-slip earthquakes (e.g., SHEN *et al*., 1994; REILINGER *et al*., 2000). Although many discrete creep events may be involved in the afterslip process, it can be modeled by a single slip event using an elastic dislocation theory similar with the coseismic slip inversions, since these aseismic events occur within a relatively short time period (SHEU and S$_{HIEH}$, 2004).

The method proposed by WANG *et al*. (2009) was used in the afterslip inversion of the Kunlun earthquake. Similar with previous methods on the slip distribution inversion, the relation between surface observation and the fault slips can be expressed when the fault geometry is fixed as expressed by:

$$y = Gb, \tag{1}$$

where, G is the Green function, which is calculated using the dislocation theory in the elastic half-space or layered earth model; b is the slip of sub-faults; and y denotes the ground observation. In order to obtain the slip model with high resolution, the fault plane is generally discretized into many sub-faults. However, when the unknown slip parameters of the sub-faults become more than the observations, the equation becomes underdetermined. Therefore, a priori or artificial constraint is required to avoid unphysically large variations in the slip distribution.

A general method used in previous studies (e.g., MATTHEWS and SEGALL, 1993; HSU *et al*., 2002; LASSERRE *et al*., 2005) to add artificial constraint considered smoothing the slip distribution mathematically. WANG *et al*. (2009) stated that the slip models can be constrained to those with appropriate roughness in the stress drop. The objective function can be expressed as:

$$F(b) = \| Gb - y \| + \alpha^2 \| H\tau \|^2, \tag{2}$$

where, τ is the shear stress drop caused by the distributed slip on the whole fault plane, H is the finite difference approximation of the Laplacian operator multiplied by a weighting factor relating to the slip amplitude, and α is the smoothing factor. The weighting factor is imported to the

Laplacian operator for resolving slip concentrations effectively. Generally, the maximum stress drop shows clear inverse dependence with the smoothing factor. If the maximum stress drop can be estimated from other techniques, such as teleseismic inversions, we can obtain the appropriate smoothing factor by fitting the estimation of the maximum stress drop. However, in this study, a general way to fix the smoothing factor was to choose the reasonable value from the trade-off curve with misfit plotted as a function of the roughness of the stress drop. As shown in Fig. 3, we chose a smoothing factor of $\alpha = 0.15$ at the point of the maximum curvature to solve our final afterslip model; a higher α resulted in significant worse misfit, while a lower α did not improve the misfit clearly. A detailed description about the inversion method will be presented in a separate paper and we just explain it briefly in this paper.

An afterslip often occurs on the coseismic rupture plane or on its surrounding area with similar slip direction (PERFETTINI and AVOUAC, 2004; HSU *et al*., 2002). Therefore, an extended fault plane should be considered in the afterslip inversion. In this paper, the fault geometry was constructed with the same geometrical parameters as those used in the coseismic slip model (LASSERRE *et al*., 2005). However, the fault plane was extended to a depth of 70 km, which can possibly reach the bottom of the crust (WITTLINGER *et al*., 1996). In addition, the eastern end of the fault was prolonged by 50 km. There were 1,386 fault patches in the afterslip model with almost the same size of 5 km×5 km. The slips were fixed in left-lateral strike direction, consistent with that used in the coseismic slip model.

Figure 2
Figure 3

As can be seen from Fig. 2b, the inverted afterslip was concentrated in the central section of the fault, although there were clear afterslips with a magnitude of ~0.25 m occurring in the deep patches of the eastern section. More importantly, this inversion result showed that widely distributed afterslips occurred at the down extension of the coseismic slip area. This is required to explain the far-field postseismic displacements. With a maximum of up to 0.45 m in the first four months, the afterslip penetrated into the lower crust to a depth of 70 km in the central section. Comparing this with the GPS measurements (Fig. 4a), the fit between the prediction and the observation became worse with increased distances from the fault, even though the fault was extended to 70 km. This phenomenon can be explained by the fact that there are other deep

processes driving the far-field postseismic deformation.

Figure 4

4. Viscoelastic Relaxation Model

4.1. Method

In this paper, a Maxwell body and a standard linear solid were used to investigate the extent to which the postseismic deformations in the initial four months can be explained by the viscoelastic relaxation of the lower crust and the upper mantle.

The Maxwell body is a relatively simple viscous-elastic system, which is represented by an elastic element in series with a viscous element (Fig. 5). The constitutive relation governing a Maxwell body is expressed by:

$$\dot{\varepsilon} = \dot{\sigma} / \mu + \sigma / \eta . \tag{3}$$

Considering a constant stress load, σ_0, the strain can be obtained by:

$$\varepsilon = \sigma_0 / \mu + \sigma_0 / \tau \quad , \tag{4}$$

where, $\tau = \eta / \mu$ is the Maxwell time. It can be noted that when the Maxwell solid is totally relaxed, its effective shear strength becomes zero.

An alternative rheological model used in this study is a standard linear solid (Fig. 5), which consists of a Kelvin element in series with an elastic element. The governing equation of this standard linear solid can be expressed as:

$$\sigma(\frac{1}{\mu_e} + \frac{1}{\mu_k}) + \dot{\sigma}\frac{\eta}{\mu_e \mu_k} = \varepsilon + \frac{\eta}{\mu_k}\dot{\varepsilon} . \tag{5}$$

Given a constant stress load, σ_0, the strain can be obtained by:

$$\varepsilon = -\frac{\sigma_0}{\mu_k}\exp(-\frac{\mu_k t}{\eta}) + \sigma_0(\frac{1}{\mu_e} + \frac{1}{\mu_k}) . \tag{6}$$

Compared with the Maxwell solid, the fully relaxed standard linear solid has a long-term non-zero effective strength of $\mu' = \frac{\mu_k \mu_e}{\mu_k + \mu_e}$. In addition, with two relaxation times $\tau_k = \frac{\eta}{\mu_k}$ and $\tau_s = \frac{\eta}{\mu_k + \mu_e}$, the standard linear solid has been proven to be a medium that can model both the rapid initial response and the subsequent slower response (RYDER *et al*., 2007).

Figure 5
Figure 6

The numerical code PSGRN/PSCMP (WANG *et al*., 2006) was adopted to model the viscoelastic relaxation of the Kunlun earthquake. This code can compute time-dependent postseismic deformations for a layered crust model and takes the coupling between the deformation and the gravity field of the earth into account; this has been proven to be effective and stable in viscoelastic relaxation modeling (LORENZO-MARTÍN *et al*., 2006; WANG *et al*., 2009). The grid-search method was also adopted to find the best-fitting rheological parameters.

4.2. Maxwell Model

We used a layered earth model, in which the physical parameters of each layer were inferred from the seismic profile results across the eastern Kunlun fault (WU *et al*., 1991) (Fig. 6). The thickness of the elastic upper crust was determined from the concentration of 95% of regional earthquakes (DENG *et al*., 1999), which was fixed at 32 km based from this region's recorded earthquakes in the past 30 years according to data obtained from the China Earthquake Data Center (CEDC) (http://data.earthquake.cn). The coseismic slip model derived by LASSERRE *et al*., (2005) from the InSAR data was adopted as the driving source of the viscoelastic relaxation. Therefore, the only free parameter left in the Maxwell body is the viscosity. Two different models were built due to the complexity and non-uniqueness of the viscoelastic relaxation. First, we considered a simple model with a Maxwell half-space lower crust beneath an elastic upper crust (E-M). Afterwards, a relatively complex model was built, consisting of an elastic upper crust and a Maxwell lower crust overlying a Maxwell upper mantle (E-M-M). The viscosities of the lower crust and the upper mantle in the two models were allowed to vary between 1×10^{17} Pa s and 1×10^{21} Pa s.

As shown by the results in Figs. 7a and 7b, both the E-M-M and E-M models can give a strong constraint in the viscosity within the lower crust. However, the viscosity of the upper mantle cannot be determined well in the E-M-M model. The best-fitting viscosity of the lower crust in the E-M-M model is close to 5×10^{17} Pa s, which is consistent with the search result in the E-M model. However, based on the comparison between the observation and the prediction of the best-fitting E-M-M model (Fig. 4b), we found that the predicted displacements cannot match the observation well, especially at sites very close to and far from the fault. Moreover, the deformation pattern of the prediction showed significant contrast compared with that of the observation.

Figure 7

4.3. Standard Linear Solid Model

To investigate the possibility of the viscoelastic relaxation effect, we tried a standard linear solid (SLS), another viscoelastic medium which is slightly more complicated than the Maxwell solid. Three parameters are included in a standard linear solid: the viscosity η, the unrelaxed shear modulus μ_e, and the shear modulus μ_k. The unrelaxed shear modulus μ_e can be inferred from the layered earth model. Meanwhile, the shear modulusμ_e can relate to the shear modulusμ_e using a coefficient α, which denotes the ratio between the effective and the unrelaxed shear modulus. This can be defined by:

$$\alpha = \frac{\mu_k}{\mu_k + \mu_e}. \tag{7}$$

Therefore, only two free parameters, η and α, were left in the standard linear model. The standard linear solid transforms to the Maxwell solid when$\alpha\to0$ (i.e., when $\mu_k\to0$). In this section, only a model consisting of a standard linear solid half-space lower crust beneath an elastic upper crust (E-S) was considered. The misfit-viscosity curves with various α and η are shown in Fig. 7c. The overall best-fitting viscosity of the lower crust is ~6×10^{17} Pa s, which is close to the best-fitting viscosity in the E-M model. The best-fitting coefficient α in the E-S model cannot be determined clearly, although a low value of 0.2 is preferred by the data. In addition, the prediction of the best-fitting E-S model has a similar pattern compared with that of the E-M and E-M-M models, which is clearly in contrast to the observation.

5. Combined Model

The investigations above indicate that neither afterslip nor viscoelastic relaxation can best interpret the observed postseismic displacements independently. For instance, the afterslip model can only match near-field displacements but not far-field displacements, even if the fault is extended to a depth of 70 km. On the other hand, the viscoelastic relaxation model cannot match the observation either in the near or far field. Therefore, we tried an alternative method of combining the afterslip and viscoelastic relaxation effects to better interpret the postseismic displacements of the Kunlun earthquake.

The combined model, consisting of both the afterslip and viscoelastic relaxation effects, was established through the following steps. First, we obtained the misfits between the observation and the prediction of the E-M-M viscoelastic model at each grid point; this step has been done in section 4.2. Second, based on the misfits from the first step, we inverted the afterslip at every turn to investigate whether or not it can explain the residual. Finally, based on the weighted root mean square (WRMS) error from the second step, the best-fitting rheological parameters in the E-M-M model were obtained using the grid-search method. The weights were set to become larger along with increasing distance. This is based on the fact that the effects of the viscoelastic relaxation on far-field postseismic displacements are larger than that of the near-field postseismic displacements from the results above. Furthermore, the two processes were assumed to be independent as the viscoelastic relaxation caused by afterslip is negligible (SHEU and S_{HIEH}, 2004).

The grid-search result of the combined model is shown in Fig. 7d, in which it can be seen that the WRMS varies as a function of the viscosities in the E-M-M model. We found that a “weak” upper mantle with viscosity of ~1×10^{18} Pa s is required in order to explain the far-field postseismic deformations. However, the viscosity of the lower crust cannot be determined well in the combined model. The misfits vary when the viscosity of the upper mantle changes at low viscosities, thus there is a stronger lower bound to the apparent viscosity than the upper bound. Based on the postseismic displacements after removing the viscoelastic relaxation effect, the optimal afterslip distribution (Fig. 2c) was inverted using the same method as that used in section 3. Comparing the afterslip distribution in the combined model and that in the afterslip model (Figs. 2c and 2b), we found that afterslip focused more clearly at a shallower depth after removing the effect of viscoelastic relaxation. In addition, the combined model (Fig. 3c) can better match the postseismic deformations than the model in which the afterslip and the viscoelastic relaxation

effects are working independently.

6. Discussion

Based on the modeling results, we inferred that afterslip is the dominant mechanism involved in postseismic displacements in the near field, while viscoelastic relaxation is responsible for the far-field postseismic deformation. Using the postseismic displacements after removing the viscoelastic relaxation effect, the afterslip distribution was obtained in the combined model, which showed a clear difference from the afterslip model that worked independently. Compared with the coseismic slip model (LASSERRE *et al*., 2005), whose slip is mostly concentrated at a depth of less than 20 km, an important characteristic of the inverted afterslip is that it can penetrate into deeper patches, although there are patches with clear afterslips occurring at a shallower depth in the central section of the fault. The maximum afterslip in the first four months reached about ~0.4 m, which is 5% of the maximum of the coseismic slip (~8 m). However, the moment released by the afterslip model is almost 40% of that released by the main shock, which can correspond to an earthquake with a moment magnitude close to 7.4. The afterslip in the western section of the fault seemed to be negligible, which could be due to the poor data coverage in this region.

The distribution of the afterslip in the first four months is consistent with that of the aftershocks that occurred during this time period. The aftershocks are mostly concentrated at the eastern section of the fault plane, where the afterslip is also larger compared to the other areas (Fig. 2c). As discovered by CAKIR *et al*. (2003) on the Izmit earthquake and HSU *et al*. (2002) on the Chi-Chi earthquake, the energy induced by coseismic stress loading is generally released by aftershocks or aseismic afterslips. As the GPS data in this study were collected from campaign-surveyed stations, we cannot isolate the deformation caused by large aftershocks since the postseismic deformation might include some displacements that were induced by aftershocks. This can probably explain the similar distribution of the afterslip and the aftershocks. More importantly, since significant afterslip and aftershocks occurred in the eastern section of the Kunlun fault, it is highly probable that the fault activity has migrated from west to east. However, some doubts exist regarding this extrapolation since the postseismic observation is just one profile across the fault. From Fig. 2b, the slip may naturally be concentrated at the area close to the GPS profile (afterslip concentration near sites BDGD and KLGD). In addition, this poor data coverage

may induce poor resolution on the slip distribution, especially on the slip of patches along the extension of the fault.

Constrained by displacement time series on four GPS stations, ZHANG *et al*. (2007) used the Maxwell solid and posited that the viscosity of the lower crust is in the order of ~10^{17} Pa s, which is consistent with the result we inferred from the E-M model (Fig. 7a). SHAO *et al*. (2008) considered the lateral difference of the extent of displacements decreasing toward the north and south of the fault and pointed out that the transient viscosities of the lower crust are 5.0×10^{17} and 9.0×10^{18} Pa s in the south and north sides of the Kunlun fault, respectively. However, both studies only considered the contribution of the relaxation of the lower crust and did not take into account the effects of afterslip and the relaxation of the upper mantle. In contrast, our results showed that near-field and far-field postseismic displacements are mainly caused by afterslip and the relaxation of the upper mantle, respectively. For instance, we found that the best-fitting viscosity of the lower crust is ~5.0×10^{17} Pa s in the E-M and E-M-M models (Figs. 7a and 7b), which is close to the results obtained by ZHANG *et al*. (2007) and SHAO *et al*. (2008). However, when considering the afterslip effect, the combined model can only indicate a weak upper mantle with viscosity of close to 1.0×10^{18} Pa s. In addition, the viscosity of the lower crust cannot be well constrained, thus showing significant discrepancy with the previous results. This indicates that by ignoring the contribution of afterslip, previous models seem to have overestimated the effect of the viscoelastic relaxation and have induced a low viscosity of the lower crust.

However, it should be considered that there might have been a trade-off between afterslip and the viscosity of the lower crust of the combined model due to the similar deformation pattern produced by the two mechanisms. Moreover, there are many parameters in the afterslip model, while only a single parameter is associated with the viscosity of the lower crust in the E-M-M model. Thus, the weight of the afterslip model is perhaps larger than that of the E-M-M model in the inversion calculation. This is probably the reason why we cannot obtain a well-determined lower crust viscosity in the combined model.

RYDER *et al*. (2007) demonstrated that zones of higher conductivity correlate to a first-order approximation with zones of lower viscosity, although there is no direct evidence proving the equivalence of higher conductivity and lower viscosity. Magnetotelluric investigations (WEI *et al*., 2001) across the eastern Kunlun fault implied that the conductive zone in northern Tibet might extend to greater depth than in southern Tibet. In addition, the conductivity of the upper mantle in

the Qiangtang area is larger than that in the lower crust. Therefore, it is plausible that the viscosity of the upper mantle is lower than that in the lower crust based on the magnetotelluric study. This provides support to the results we inferred from postseismic studies. In addition, the lower viscosity of the upper mantle is consistent with a region of low seismic velocities and high attenuation in northern Tibet (OWENS and ZANDT, 1997).

Figure 8

Figure 8 shows the comparison between the observed displacement time series at four GPS sites, as well as that predicted from the viscoelastic relaxation of the lower crust and the upper mantle in the combined model. Based on these, we found that only a small part of the observed displacement time series can be interpreted by viscoelastic relaxation. In addition, the contribution of the viscoelastic effect seems to increase along with the distance from the fault. For instance, the displacements induced by viscoelastic relaxation in the first four months were 43.5 and 10% of the observation at sites WDGD and BDGD, which were 95 km and 25 km far from the fault, respectively. Furthermore, the contribution of the viscoelastic relaxation effect seemed to increase with time. For example, the displacements in the succeeding six months following the initial four months were 70.5 and 13.5% of the observation at sites WDGD and BDGD, respectively. This phenomenon indicates that the contribution of the afterslip effect decreases rapidly relative to the viscoelastic relaxation effect. Generally, the predictions of the combined model (red curves) can fit the observations reasonably well, except for site JB30, which is intricate and may be caused by local tectonic movement after excluding the effect of the aftershock.

In this paper, we only focused on afterslip and viscoelastic relaxation. However, other mechanisms might be active, such as the poroelastic rebound and the non-linear viscoelastic flow. Many studies (PELTZER *et al.*, 1998; JÓNSSON *et al.*, 2003) indicated that the poroelastic rebound generally induce surface deformation within a small scale of 10–30 km. In the case of the Kunlun earthquake, most of the GPS stations are located beyond the plausible scale induced by the poroelastic rebound and might not be caused by this mechanism. Another possible mechanism is the power-law flow, which is found to be a good reason for explaining the postseismic deformation following the Hector Mine and Landers earthquakes in California and the Denali earthquake in Alaska (FREED and BÜRGMANN, 2004; FREED *et al.*, 2006). Due to the short time

coverage of the postseismic observation, we did not explore the possibility of this mechanism in this study.

In addition, the model used in this study is relatively simple, although many factors have been considered as well. For instance, the thickness of the uppermost elastic layer was fixed in the viscoelastic modeling, which perhaps cannot be determined by simply using the regional source depth and may show trade-offs with the viscosity of the underlying layers. In addition, we did not consider the lateral variation of the medium on each side of the fault.

7. Conclusion

Constrained by postseismic deformations in the initial four months following the Kunlun earthquake, we found that afterslip is the dominant mechanism for postseismic displacements in the near field, while viscoelastic relaxation of the lower crust and the upper mantle is responsible for postseismic displacements that are far from the fault. A combined model consisting of the afterslip and viscoelastic relaxation effects can explain postseismic deformation in both the near and far fields. The maximum afterslip of ~0.4 m was found to be concentrated in the central section of the fault plane, and the moment released by the afterslip was almost 40% of that released by the main shock, which can correspond to an earthquake with a moment magnitude close to 7.4. With most afterslip occurring in and around the coseismic rupture area, a clear afterslip was also found on the east section of the rupture plane. Combined with the distribution of the aftershocks that occurred during this time period, we inferred that the fault activity might have migrated from west to east. Using the Maxwell solid, the final best-fitting viscoelastic relaxation model showed that a weak upper mantle with a viscosity of ~1.0×10^{18} Pa s, and possibly a "strong" lower crust with a viscosity larger than 1.0×10^{18} Pa s are required in order to explain both the near- and far-field postseismic displacements. Without considering the significant effect of afterslip in the near field, the inferred viscoelastic lower crust with a viscosity of ~10^{17} Pa s in previous postseismic studies of the Kunlun earthquake might be unreasonable. The new insights derived from the postseismic modeling have important implications for gaining a further understanding of the rheological structure of Tibet and the dynamic evolution of the Kunlun fault.

Acknowledgements

We thank Dr. Y. J. Hsu for valuable suggestions that contribute to the improvement of the

initial manuscript. We are grateful to Dr. C. Lasserre for kindly providing the digital coseismic slip model of the Kunlun earthquake. We thank two anonymous reviewers and the editor Dr. E. Carminati for their valuable comments, and Dr. J. X. Cai for carefully polishing up the paper. This study was supported by the Knowledge Innovation Program of Chinese Academy of Sciences (KZCX3-SW-153) and National Natural Science Foundation of China (40474028; 40604004).The figures were made using free GMT (Generic Mapping Tools) software (Wessel and Smith, 1991).

REFERENCES

CAKIR, Z., CHABLIER, J. B., ARMIJO, R., MEYER, B., BARKA, A., and PELTZER, G. (2003), *Coseismic and early post-seismic slip associated with the 1999 Izmit earthquake (Turkey), from SAR interferometry and tectonic field observations*, Geophys. J. Int., *155*, 93–110.

DENG, J., GURNIS, M., KANAMORI, H., and HAUKSSON, E. (1998), *Viscoelastic flow in the lower crust after the 1992 Landers, California, earthquake*, Science, *282*, 1689-1692, doi: 10.1126/science.282.5394.1689.

DENG, J., HUDNUT, K., GURNIS, M., and HAUKSSON, E. (1999), *Stress loading from viscous flow in the lower crust and triggering of aftershocks following the 1994 Northridge, California earthquake*, Geophys. Res. Lett., *26*, 3209-3212.

FREED, A. M., and BÜRGMANN, R. (2004), *Evidence of power-law flow in the Mojave desert mantle*, Nature, *430*, 548-551, doi:10.1038/nature02784.

FREED, A. M., BÜRGMANN, R. CALAIS, E., and FREYMUELLER, J. (2006), *Stress dependent power-law flow in the upper mantle following the 2002 Denali, Alaska, earthquake*, Earth Planet. Sci. Lett., *252*, 481-489, doi:10.1016/j.epsl.2006.10.011.

FREED, A. M., BÜRGMANN, R., and HERRING, T. (2007), *Far-reaching transient motions after Mojave earthquakes require broad mantle flow beneath a strong crust*, Geophys. Res. Lett., *34*, L19302, doi:10.1029/2007GL030959.

FREED, A. M. (2007), *Afterslip (and only afterslip) following the 2004 Parkfield, California, earthquake*, Geophys. Res. Lett., *34*, L06312, doi:10.1029/2006GL029155.

HSU, Y. J., BECHOR, N., SEGALL, P., YU, S. B., KUO L. C., and MA, K. F. (2002), *Rapid afterslip following the 1999 Chi-Chi, Taiwan Earthquake*, Geophys. Res. Lett., *29*, 1754-1757, doi: 10.1029/2002 GL014967.

1 JÓNSSON, S., SEGALL, P., PEDERSEN, R., and BJÖRNSSON, G. (2003), *Post-earthquake ground*
2 *movements correlated to poro-pressure transients*, *Nature*, *424*, 179-183,
3 doi:10.1038/nature01776.

4 KLINGER, Y., XU, X., TAPPONNIER, P., WOERD, J. V., LASSERRE, C., and KING, G. (2005),
5 *High-Resolution Satellite Imagery Mapping of the Surface Rupture and Slip Distribution of the*
6 *Mw ~7.8, 14 November 2001 Kokoxili Earthquake, Kunlun Fault, Northern Tibet, China*, Bull.
7 Seism. Soc. Am., *95*, 1970-1987, doi:10.1785/0120040233.

8 LASSERRE, C., PELTZER, G., CRAMPÉ, F., KLINGER, Y., WOERD, J. V., and TAPPONNIER, P. (2005),
9 *Coseismic deformation of the 2001 Mw=7.8 Kokoxili earthquake in Tibet, measured by*
10 *synthetic aperture radar interferometry*, J. Geophys. Res., *110*, B12408, 1-17, doi:10.1029/
11 2004JB003500.

12 LIN, A. M., KIKUCHI, M., and FU, B. H. (2002), *Co-Seismic strike-slip and rupture length produced*
13 *by the 2001 Ms 8.1 central Kunlun earthquake*, Science, *296*, 2015-2017, doi: 10.1126 /science.
14 1070879.

15 LORENZO-MARTÍN, F., ROTH, F., and WANG, R. (2006), *Inversion for rheological parameters from*
16 *postseismic surface deformation associated to the 1960 Valdivia earthquake, Chile*, Geophys. J.
17 Int., *164*, doi:10.1111/j.1365-246X.2005.02803.x.

18 MATTHEWS, M., and SEGALL, P. (1993), *Statistical inversion of crustal deformation data and*
19 *estimation of the depth distribution of slip in the 1906 earthquake*, J. Geophys Res., *98*, 12,153–
20 12,163.

21 MIYAZAKI, S., SEGALL, P., FUKUDA, J., and KATO, T. (2004), *Space time distribution of afterslip*
22 *following the 2003 Tokachi-oki earthquake: Implications for variations in fault zone frictional*
23 *properties*, Geophys. Res. Lett., *31*, L06623, doi:10.1029/2003GL019410.

24 OWENS, T. J., and ZANDT, G. (1997), I*mplications of crustal property variations for models of*
25 *Tibetan plateau evolution*, Nature, *387*, 37-43, doi:10.1038/387037a0.

26 PERFETTINI, H., and AVOUAC, J. P. (2004), *Postseismic relaxation driven by brittle creep: A possible*
27 *mechanism to reconcile geodetic measurements and the decay rate of aftershocks, application*
28 *to the Chi-Chi earthquake, Taiwan*, J. Geophys. Res., *109*, B02304, doi:10.1029/2003
29 JB002488.

PELTZER, G., ROSEN, P., ROGEZ, F., and HUDNUT, K. (1998), *Poroelastic rebound along the Landers 1992 earthquake surface rupture*, J. Geophys. Res., *103*, 30,131–30,145.

POLLITZ, F. F., PELTZER, G., and BURGMANN, R. (2000), *Mobility of continental mantle: Evidence from postseismic geodetic observations following the 1992 Landers earthquake*, J. Geophys. Res., *105*, 8035-8054.

POLLITZ, F. F. (2005), *Transient rheology of the upper mantle beneath central Alaska inferred from the crustal velocity field following the 2002 Denali earthquake*, J. Geophys. Res., *110*, B08407, doi:10.1029/2005JB003672.

QIAO, X. J., WANG, Q., DU, R. L., YOU, X. Z., and TAN, K. (2002), *Characteristics of crustal deformation relating to Ms 8.1 Kunlun Earthquake*, J. Geodesy and Geodynamics, *22*, 6-11, (in Chinese).

REILINGER, R. E., ERGINTAV, S., BÜRGMANN, R., MCCLUSKY, S., LENK, O., BARKA, A., GUREKAN, O. HEARN, L., and FEIG, K. L. (2000), *Coseismic and postseismic fault slip for the 17 August 1999, M=7.5, Izmit, Turkey Earthquake*, Science, *289*, 1519-1524, doi:10.1126/science.289.5484. 1519.

REN, J. W., and WANG M. (2005), *GPS measured crustal deformation of the Ms8.1 Kunlun earthquake on Novemeber 14th 2001 in Qinghai-Xizang plateau*, Quaternary Sciences, *25*, 34-44, (in Chinese).

RYDER, I., PARSONS, B., WRIGHT, T. J., and FUNNING, G. J. (2007), *Post-seismic motion following the 1997 Manyi (Tibet) earthquake: InSAR observations and modelling*, Geophys. J. Int., *169*, 1009-1027, doi:10.1111/j.1365-246X.2006.03312.x.

SAVAGE, J. C., and SVARC, J. L. (1997), *Postseismic deformation associated with the 1992 M_w = 7.3 Landers earthquake, southern California*, J. Geophys. Res., *102*, 7565–7577.

SHAO, Z., FU, R. S., and XUE, T. X. (2008), *The numerical simulation and discussion on mechanism of post seismic deformation after Kunlun Ms 8.1 earthquake*, Chinese J. Geophys., *51*, 805-816.

SHEN, Z. K., JACKSON, D. D., FENG, Y., CLINE, M., KIM, M., FANG, P., and BOCK, Y. (1994), *Postseismic deformation following the Landers earthquake, California, 28 June 1992*, Bull. Seism. Soc. Am., *84*, 780-791.

SHEU, S. Y., and SHIEH, C. F. (2004), *Viscoelastic-afterslip concurrence: a possible mechanism in the early post-seismic deformation of the Mw 7.6, Chi-Chi (Taiwan) earthquake*, Geophys. J. Int., *159*, 1112–1124, doi:10.1111/j.1365-246X.2004.02437.x.

WANG, L., WANG, R., ROTH, F., ENESCU, B., HAINZL, S., and ERGINTAV, S. (2009), *Afterslip and viscoelastic relaxation following the 1999 M7.4 Ízmit earthquake, from GPS measurements*, Geophys. J. Int., *178*, 1220–1237, doi: 10.1111/j.1365-246X.2009.04228.x.

WANG, Q., ZHANG, P. Z., FREYMUELLER, J. T., BILHAM, R., LARSON, K. M., LAI, X., YOU, X. Z., NIU, Z. J., WU, J. C., LI,Y. X., LIU, J. N., YANG, Z. Q., and CHEN, Q. Z. (2001), *Present-day deformation in China constrained by global positioning system measurements*, Science, *294*, 574–575, DOI:10.1126/science.1063647.

WANG, R., MARTÍN, F. L., and ROTH, F. (2006), *PSGRN/PSCMP - a new code for calculating co- and post-seismic deformation, geoid and gravity changes based on the viscoelastic-gravitational dislocation theory*, Computers & Geosciences, 32, 527-541, doi:10.1016/j.cageo. 2005.08.006.

WEI, W. B., UNSWORTH, M., JONES, A. BOOKER, J., TAN, H., NELSON, D., CHEN, L., LI, S., SOLON, K., BEDROSIAN, P., JIN, S., DENG, M., LEDO, J., KAY, D., and ROBERTS, B. (2001), *Detction of widespread fluids in the Tibetan crust by magnetotelluric studies*, Science, 292, 716-718, doi: 10.1126/science.1010580.

WESSEL, P., and SMITH, W. H. F. (1991), *Free software helps map and display data*, Eos. Trans. Am. Geophys., *72*, 445–446.

WITTLINGER, G., MASSON, F., POUPINET, G., TAPPONNIER, P., JIANG, M., HERQUEL, G., GUILBERT, J., ACHAUER, U., XUE, G., SHI, D., and Lithoscope Kunlun Team (1996), *Seismic tomography of north Tibet and Kunlun: Evidence for crustal blocks and mantle velocity contrasts*. Earth Planet Sci. Lett., *139*, 263―279.

WU, G. J., GAO, R., and YU, Q. F. (1991), *Integrated investigations of the Qinghai-Tibet plateau along the Yadong-Golmud geosciences transect*, Chinese J. Geophys., *34*, 552-562 (in Chinese).

XU, X., YU, G., KLINGER, Y., TAPPONNIER, P., and WOERD, J. V. (2006), *Reevaluation of surface rupture parameters and faulting segmentation of the 2001 Kunlunshan earthquake (Mw7.8),*

northern Tibetan Plateau, China, J. Geophys. Res., *111*, B05316, doi:10.1029/2004JB003488, 2006.

ZHANG, C. J., SHI, Y. L., MA, L., and LOMNITZ, C. (2007), *A rhelolgical model of post-seismic deformation for 2001 Kunlun, China earthquake, Mw7.8*, Geofísica Internacional, *46*, 145-154.

Figure captions

Fig. 1. Tectonic setting of the Kunlun earthquake. The thick dark line corresponds to the surface rupture of the Kunlun earthquake (LASSERRE *et al*., 2005). The focal mechanism was taken from the CMT solution released by the US Geological Survey (USGS). The white arrows show the velocity vectors of the crust movement in the Eurasian frame (KLINGER *et al*., 2005). The thin dark lines are the main tectonic faults in the Tibet Plateau.

Fig. 2. (a) The three-dimensional coseismic slip distribution on the extended fault plane, which was inverted from the InSAR observation by LASSERRE *et al*. (2005). (b) The afterslip model inverted from the observed postseismic displacements without removing the viscoelastic effect. (c) The afterslip in the combined model, i.e., considering the contribution of the viscoelastic effect. The white circles represent the aftershocks (M >= 3) that occurred during the initial four months, according to data released by the China Earthquake Data Center (CEDC) (http://data.earthquake.cn). The area between the two white lines in Fig 2. (b) and (c) denotes the coverage of the GPS data along the strike direction.

Fig. 3. Trade-off curve with data misfit plotted as a function of the model roughness of the stress drop. Note that the misfit is the relative residual.

Fig. 4. Comparison between the observed and the predicted postseismic displacements of the Kunlun earthquake from (a) the afterslip model inverted using the optimal smoothing factor fixed in Fig. 3, (b) the best-fitting E-M-M vicoelastic relaxation model, and (c) the combined model which considers both the afterslip and viscoelastic relaxation effects. Error ellipses indicate 95% confidence intervals.

Fig. 5. Schematic diagrams of the Maxwell body and the standard linear solid body used in our study. The shear modulus in the Maxwell body is represented by μ, whileμ_e and μ_k are the unrelaxed shear and the relaxed shear modulus, respectively. The viscosity in the two elements is represented by η.

Fig. 6. layered earth model of the northeast Tibet Plateau used in this study (WU *et al*., 1991): (a)

is the seismic velocity; (b) is the density; and (c) is the inferred Yong's modulus. The grey lines denote the boundaries between the upper crust, lower crust, and the upper mantle.

Fig. 7. Misfit variation in the different viscoelastic models: (a) E-M model, (b) E-M-M model, (c) E-S model with different α, and (d) the combined model. From (a) and (c), it is clear that the standard linear solid is equivalent to the Maxwell solid when the coefficient α becomes zero.

Fig. 8. Comparisons between the observed and the predicted displacement time series in the E-W direction. The various observed time series are denoted by the black dots with one sigma error bars. The solid black curves are the exponential fits with different relaxation time. The red curves represent the predictions of the combined model, in which the contribution of the afterslip is estimated from empirical relationship like the Omori's law about the temporal distribution of the aftershock. The dashed black curves are the time-dependent displacements predicted by the viscoelastic relaxation effect in the combined model. The dark arrows are the contribution induced by the best-fitting afterslip model.

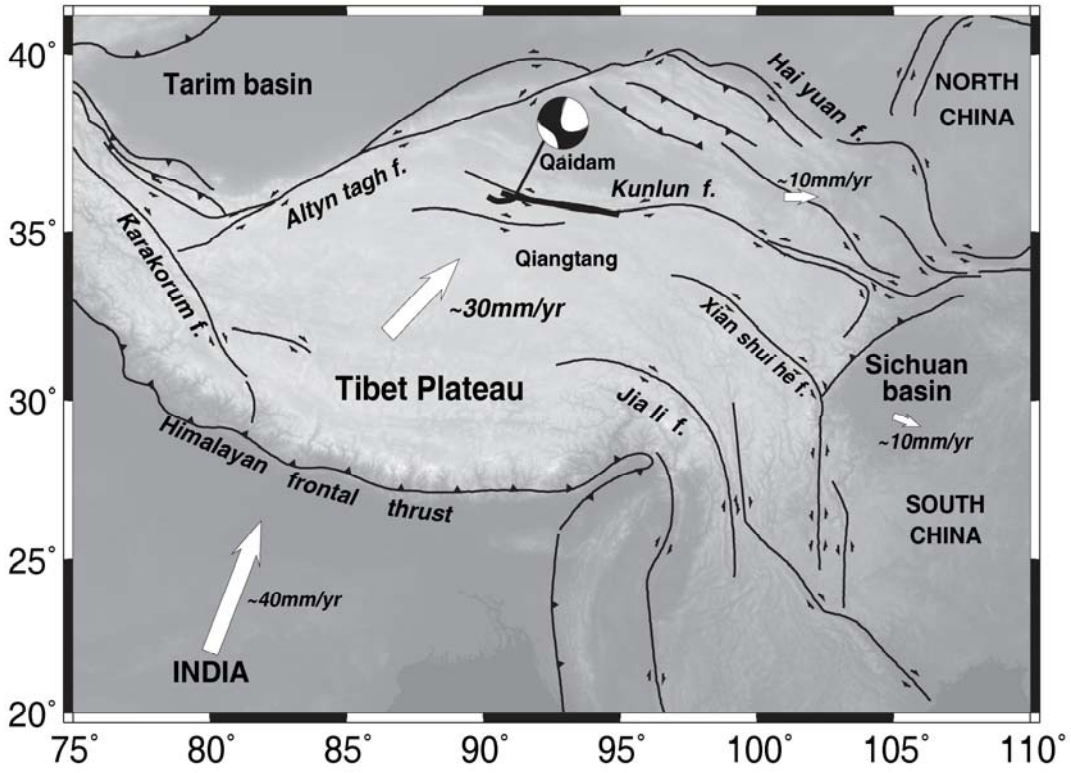
Tarim basin
Hai yuan f.
NORTH
CHINA
Qaidam
Kunlun f.
~10mm/yr
Altyn tagh f.
Karakorum f.
Qiangtang
~30mm/yr
Xian shui he f.
Sichuan
basin
Tibet Plateau
Jia li f.
~10mm/yr
Himalayan frontal thrust
SOUTH
CHINA
~40mm/yr
INDIA
40°
35°
30°
25°
20°
75°
80°
85°
90°
95°
100°
105°
110°

Figure 1

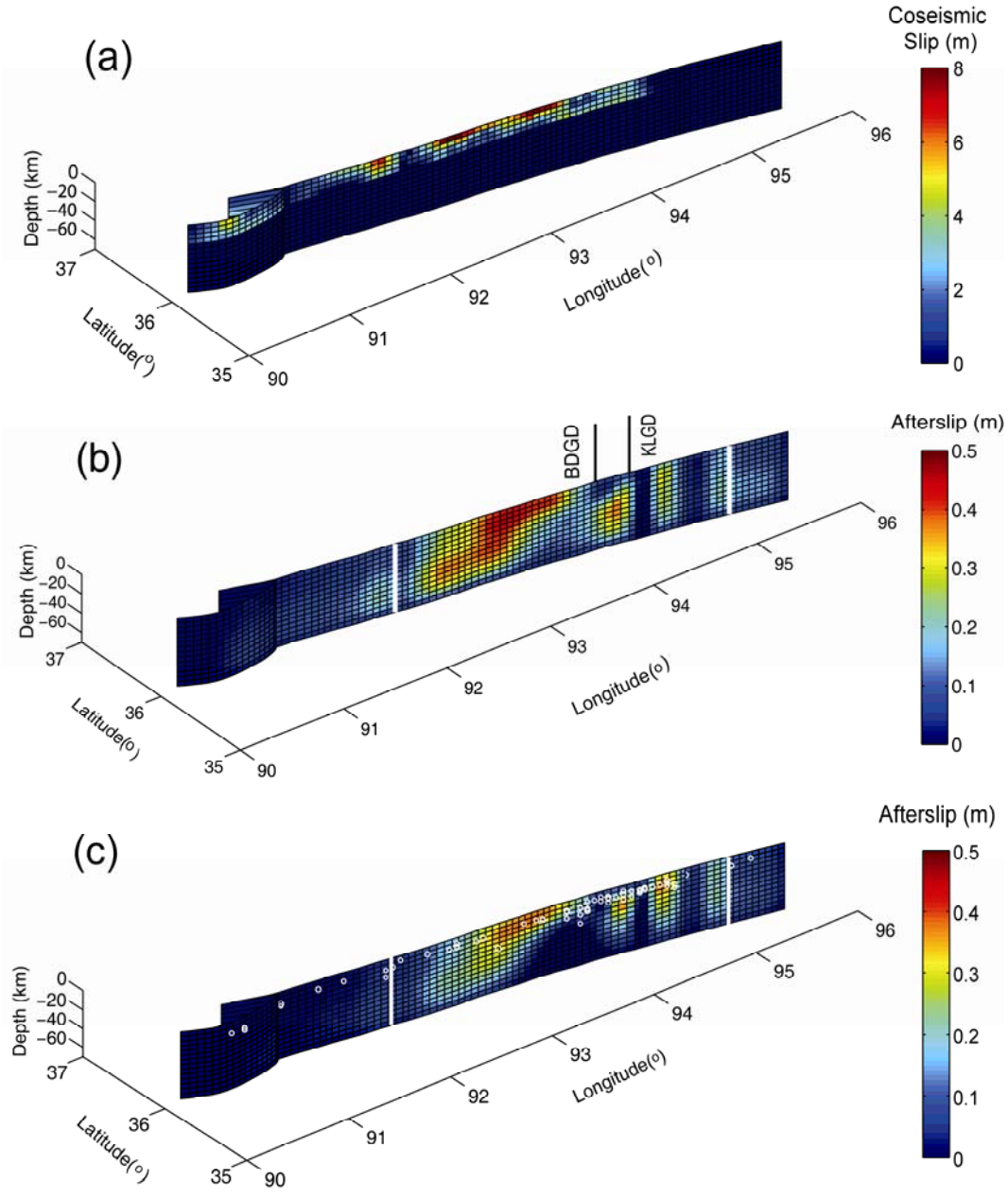
(a)
Coseismic
Slip (m)
8
6
4
2
0
Depth (km)
0
−20
−40
−60
37
36
35
Latitude(°)
90
91
92
93
94
95
96
Longitude(°)
(b)
BDGD
KLGD
Afterslip (m)
0.5
0.4
0.3
0.2
0.1
0
Depth (km)
0
−20
−40
−60
37
36
35
Latitude(°)
90
91
92
93
94
95
96
Longitude(°)
(c)
Afterslip (m)
0.5
0.4
0.3
0.2
0.1
0
Depth (km)
0
−20
−40
−60
37
36
35
Latitude(°)
90
91
92
93
94
95
96
Longitude(°)

Figure 2

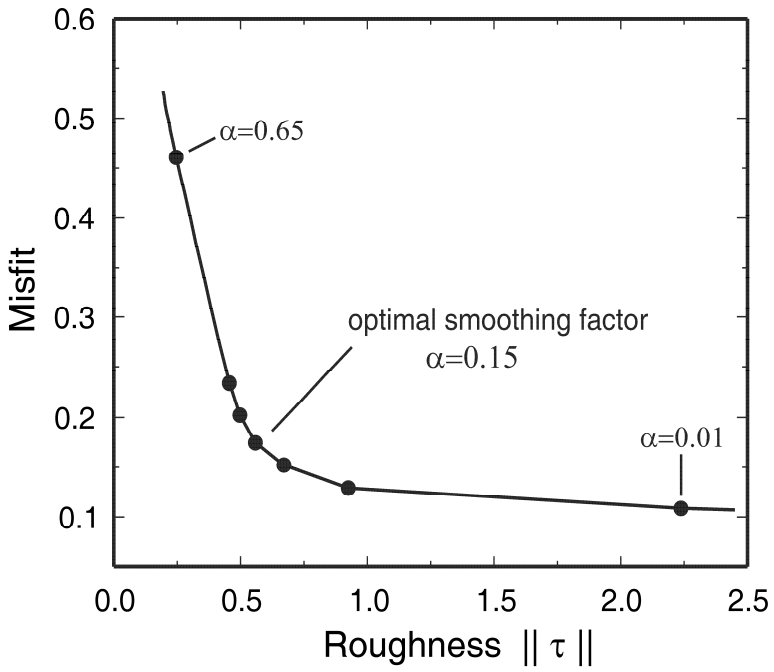
0.6
0.5
0.4
0.3
0.2
0.1
Misfit
α=0.65
optimal smoothing factor
α=0.15
α=0.01
0.0
0.5
1.0
1.5
2.0
2.5
Roughness || τ ||

Figure 3

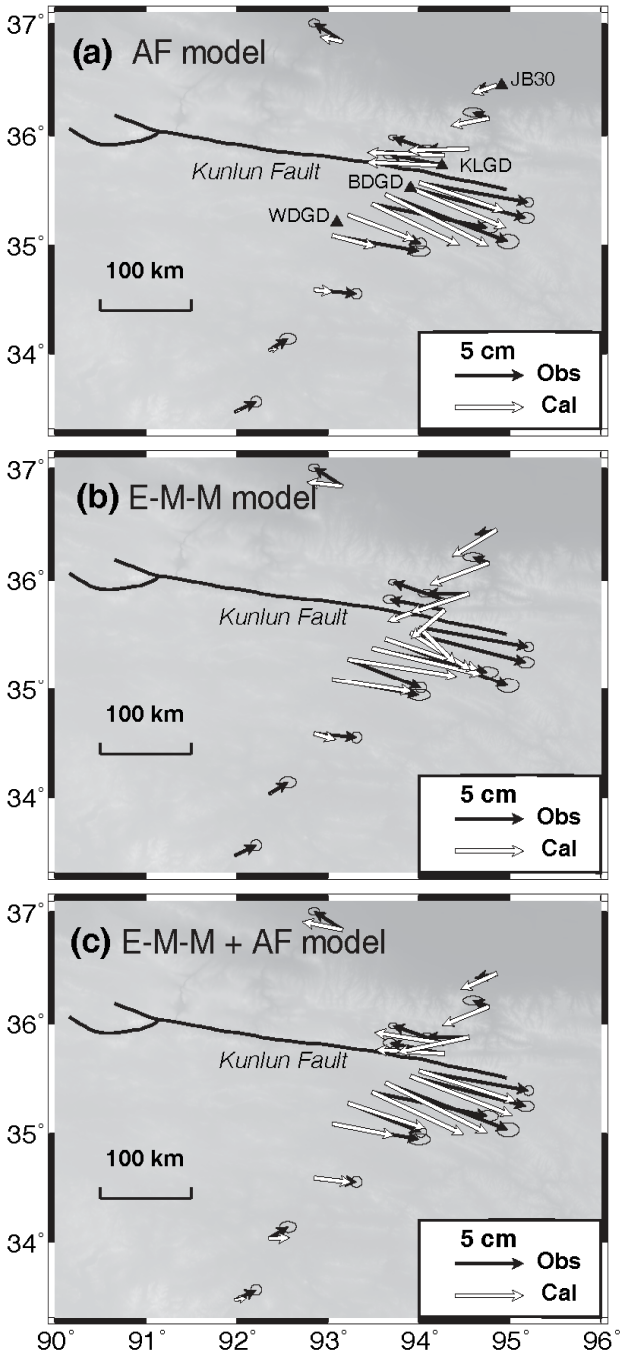
(a) AF model
JB30
KLGD
BDGD
WDGD
Kunlun Fault
100 km
5 cm
Obs
Cal
(b) E-M-M model
Kunlun Fault
100 km
5 cm
Obs
Cal
(c) E-M-M + AF model
Kunlun Fault
100 km
5 cm
Obs
Cal
37°
36°
35°
34°
90°
91°
92°
93°
94°
95°
96°

Figure 4

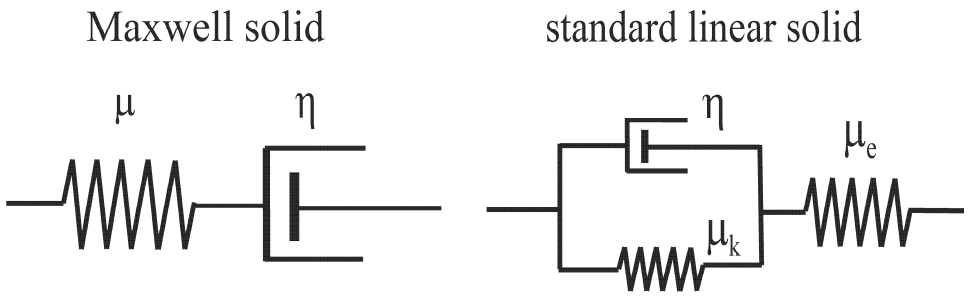

Figure 5

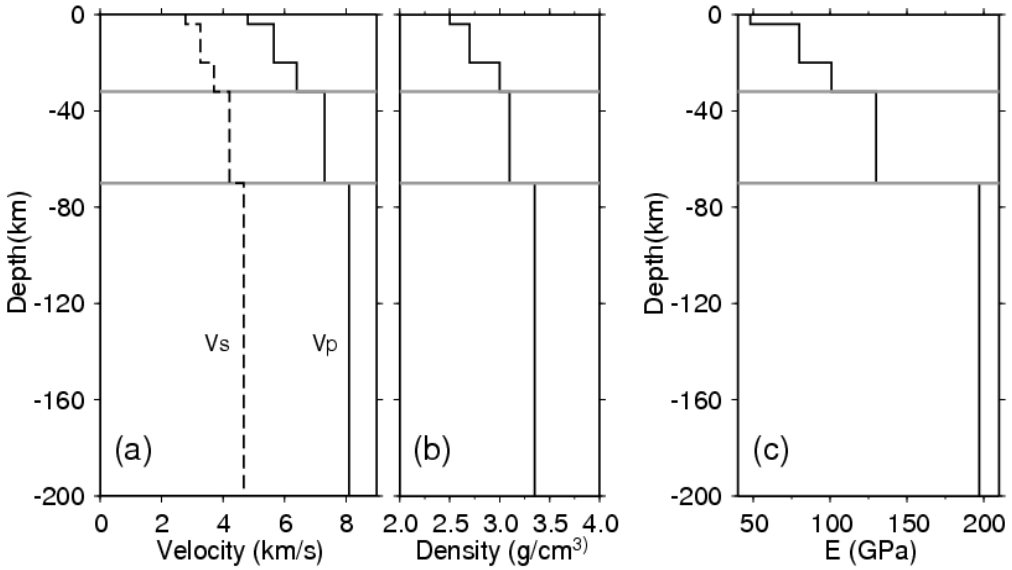

Figure 6

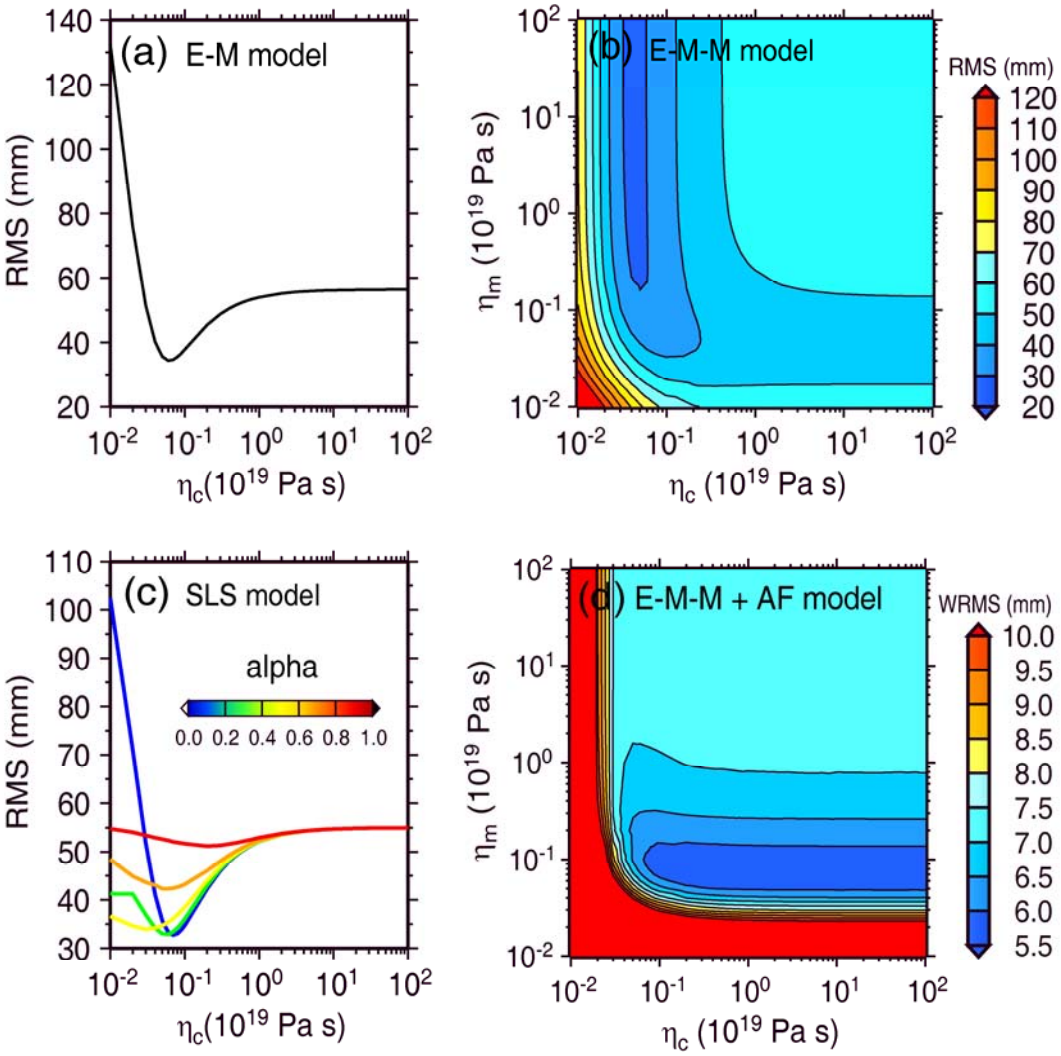
(a) E-M model
RMS (mm)
η_c(10^{19} Pa s)
(b) E-M-M model
RMS (mm)
η_m (10^{19} Pa s)
η_c (10^{19} Pa s)
(c) SLS model
alpha
0.0 0.2 0.4 0.6 0.8 1.0
RMS (mm)
η_c(10^{19} Pa s)
(d) E-M-M + AF model
WRMS (mm)
η_m (10^{19} Pa s)
η_c (10^{19} Pa s)

Figure 7

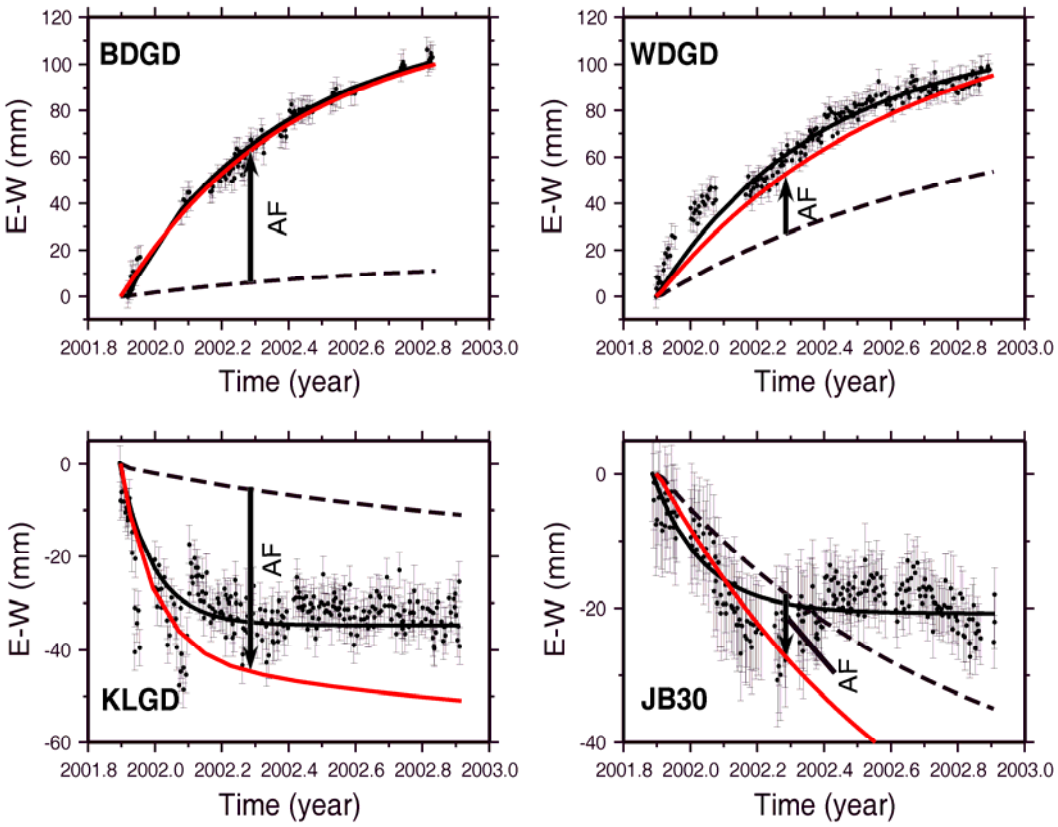
BDGD
WDGD
KLGD
JB30
AF
E-W (mm)
Time (year)
2001.8 2002.0 2002.2 2002.4 2002.6 2002.8 2003.0

Figure 8